

# Potentiostatic synthesis of polyaniline zinc and iron oxide composites for energy storage applications

Imran Khan<sup>a,c</sup>, Anwar ul Haq Ali Shah<sup>a,\*</sup>, Salma Bilal<sup>b</sup>, Philipp Röse<sup>c,\*</sup>

<sup>a</sup> Institute of Chemical Sciences, University of Peshawar, Peshawar, Khyber Pakhtunkhwa 25120, Pakistan

<sup>b</sup> National Centre of Excellence in Physical Chemistry, University of Peshawar, Peshawar, Khyber Pakhtunkhwa 25120, Pakistan

<sup>c</sup> Institute for Applied Materials - Electrochemical Technologies, Karlsruhe Institute of Technology, Karlsruhe 76131, Germany

## ARTICLE INFO

### Keywords:

Conductive polymer  
Functionalized polyaniline  
Electrosynthesis  
Metal oxide nanoparticles  
Energy storage

## ABSTRACT

This study introduces an efficient potentiostatic method to enhance the energy storage performance of polyaniline (PN) by synthesizing PN@ZnO (PNZ), PN@Fe<sub>2</sub>O<sub>3</sub> (PNF), and PN@ZnFe<sub>2</sub>O<sub>4</sub> (PNZF) hybrid electrodes with defined porous morphology. The precise selection and control of the working potential during electropolymerization and metal oxide integration using the linear sweep voltammetry was key for synthesizing the polymer hybrid electrodes reproducible and with defined composition and structure. The PNZF electrode demonstrated the highest specific capacitances of 816 F g<sup>-1</sup> and 791.3 F g<sup>-1</sup> at a scan rate of 5 mV s<sup>-1</sup> and 1.0 A g<sup>-1</sup> current density, along with high power density and energy density of 1058.4 W kg<sup>-1</sup> and 136.4 Wh kg<sup>-1</sup>, and with excellent stability retaining 90 % over 4000 cycles. We could attribute the excellent performance to a low charge transfer resistance of 25.0 Ω, a predominantly surface-controlled charge storage mechanism, and a porous morphology with uniform distribution of ZnFe<sub>2</sub>O<sub>4</sub> particles in the polymer network, all resulting from the electrochemical synthesis method. Our study provides valuable and new insights into the structural, optical, and electrochemical properties of PN composites, particularly PNZF.

## 1. Introduction

Supercapacitors (SC) with an energy density (>20 Wh/kg) and a power density (>2 kW/kg) are a key element of the current sustainable energy transition. [1]. They excel in energy storage performance and boast fast rechargeability, exceptional thermal stability, and prolonged service life (>10<sup>5</sup> cycles). These qualities make them highly versatile across various technologies, including hybrid automobile vehicles, uninterruptable power supply systems, and electronic devices [2,3].

Various electrode materials used in SCs range from transition metal oxides and carbon compounds such as graphene and carbon nanotubes (CNTs) to conductive polymers such as polyaniline (PN), polythiophene (PTh) and polypyrrole (PPy) and their composite blends [4–6]. Polyaniline has proven to be a promising choice among the various SCs in recent decades due to its low mass density, ease of synthesis, high pseudocapacity, high flexibility, low cost and high conductivity. However, pristine PN electrodes are characterized by high volume expansion and contraction with low cyclic stability and mechanical strength during multiple charge-discharge cycles. Numerous efforts have been made to overcome these drawbacks, including blending hetero-materials like

graphene oxides and CNTs and active metal oxides such as Fe<sub>2</sub>O<sub>3</sub>, ZnO, NiO, MnO<sub>2</sub>, CuO, SnO<sub>2</sub>, and TiO<sub>2</sub>. Among hetero-materials, metal oxides have shown promising results as they not only stabilize the structure but also improve the capacitive charge storage. For instance, Gautam et al. synthesized PN-NiO composites with 89 % retention in capacitance over 5000 cycles [7]. Usman et al. reported Fe/Ni codoped PN composite with Co<sub>3</sub>O<sub>4</sub>, achieving 84 % retention after 2000 cycles [8]. Varghees et al. used MnO<sub>2</sub>/SnO<sub>2</sub> nanoparticles for PN composite and achieved 97.7 % retention over 5000 cycles [9], while Azimov et al. reported 90.1 % retention in capacitance over 3000 cycles using α-Fe<sub>2</sub>O<sub>3</sub> for PN composite [10]. The resulting composites demonstrated a positive approach toward cyclic stability.

However, challenges like metal oxide agglomerations during chemical synthesis, lack of control over morphology and porosity, chances of impurity and by-product formation, and expensive precursors used like ammonium peroxy-disulfide or benzoyl peroxides as oxidant, cyclohexane, or isopropanol as emulsifier and polyvinyl amide (PVA) as binder have switched the researcher's attention toward electrochemical synthesis.

Electrochemical procedures have recently gained significant

\* Corresponding authors.

E-mail addresses: [anwarulhaqalishah@uop.edu.pk](mailto:anwarulhaqalishah@uop.edu.pk) (A.H.A. Shah), [philipp.roese@kit.edu](mailto:philipp.roese@kit.edu) (P. Röse).

<https://doi.org/10.1016/j.synthmet.2024.117784>

Received 27 June 2024; Received in revised form 4 November 2024; Accepted 12 November 2024

Available online 14 November 2024

0379-6779/© 2024 The Author(s). Published by Elsevier B.V. This is an open access article under the CC BY license (<http://creativecommons.org/licenses/by/4.0/>).

attention due to their control over products, *in situ* synthesis and simultaneous characterization, large-scale production potential, and tunable electrochemical properties. Unsurprisingly, several parameters are considered while synthesizing metal oxide integrated PN hybrid electrodes to enhance energy storage performance. According to Sardana et al., the super-capacitive performance of electrochemically synthesized PN electrodes greatly depends upon fast Faradaic surface-controlled electrochemical processes [11]. Shah et al. have achieved a high specific aerial capacitance using indium tin oxide nanoparticles (ITO) integrated PN composite following the electrochemical synthesis [12]. Changing the working electrode to steel mesh by electrochemical depositing PN thin films, as reported by Mahfoz et al. [13], has achieved high power density in addition to specific capacitance. An electrochemically integrated TiO<sub>2</sub>-based PN composite reported by Maghsoudi et al. [14] has shown better electrochemical properties and specific areal capacitance than those synthesized by chemical polymerization.

This paper introduces an innovative approach for synthesizing ferrite-integrated polyaniline composites using efficient potentiostatic electrosynthesis. Compared to traditional chemical and electrochemical methods, this approach provides precise control over surface morphology, conductivity, and surface-controlled redox behavior, as demonstrated by the results. It ensures greater uniformity and consistency in composite thin films, [15] facilitates the even distribution of metal oxide nanoparticles, and enhances surface morphology by increasing the electrochemically active surface area (ECSA) – a critical factor for boosting the capacitive performance of the composites [16, 17].

Additionally, it overcomes limitations seen in other chemical methods, such as temperature control restrictions and nanoparticle segregation. For instance, CuMnFeO<sub>4</sub> integrated polyaniline composite reported by Agale et al. exhibited agglomerated metal oxide particles due to the chemical polymerization method [18]. Similarly, Singh et al. reported a specific capacitance of 758 F g<sup>-1</sup> (at a 10 mV s<sup>-1</sup> scan rate) for NiFe<sub>2</sub>O<sub>4</sub> integrated PN composite using the *in situ* chemical oxidative polymerization method, which required continuous stirring for 24 hours [19]. Soam reported a specific capacitance of 471 F g<sup>-1</sup> (at a 5 mV s<sup>-1</sup> scan rate) for zinc ferrite-integrated PN composite [20]. The relatively low capacitance in these cases can be attributed to small active surface areas and lack of porosity, likely due to conventional chemical oxidative polymerization processes.

In contrast, we hypothesize that potentiostatic electrosynthesis provides greater control over the distribution of metal oxide nanoparticles, thereby increasing the electrochemically active surface area and optimizing surface-controlled redox processes within the composite materials. This method overcomes the limitations of conventional synthesis techniques and opens new possibilities for improving the capacitive performance and stability of polyaniline-based hybrid electrodes.

Therefore, we report the precise control of optimal working potential necessary for the homogeneous distribution of metal oxide nanoparticles over the PN framework, utilizing the potentiostatic electrosynthesis. Additionally, we report the potentiostatic integration of ZnO, Fe<sub>2</sub>O<sub>3</sub>, and ZnFe<sub>2</sub>O<sub>4</sub> nanoparticles to synthesize PNZ, PNF, and PNZF hybrid electrodes, ensuring a porous morphology and a surface-controlled charge storage mechanism.

Among the different hybrid electrodes, PNZF has demonstrated the highest energy density of 136.4 Wh kg<sup>-1</sup>, at a significantly high power density of 1058.4 Wkg<sup>-1</sup>, with a specific capacitance of 791.3 F g<sup>-1</sup> at 1.0 Ag<sup>-1</sup> current density. The excellent stability, retaining 90 % over 4000 cycles with the lowest charge transfer resistance of 25.0 Ω and 82.2 % coulombic efficiency, suggests predominantly surface-controlled processes occurring at the porous surface of the hybrid electrode due to potentiostatic integration of ZnFe<sub>2</sub>O<sub>4</sub> nanoparticles. Moreover, the CV and EIS analysis confirms the minimal mass transport influence and ideal Warburg diffusion behavior of PNZF.

## 2. Experimental section

### 2.1. Chemicals

The following chemicals were used for the synthesis of hybrid electrode materials: aniline monomer (C<sub>6</sub>H<sub>5</sub>NH<sub>2</sub>, >99.5 %), sulfuric acid (H<sub>2</sub>SO<sub>4</sub>, >98 %), and dodecylbenzene sulfonic acid (DBSA) (C<sub>18</sub>H<sub>30</sub>SO<sub>3</sub>, >92 %) were purchased from Merck, ferric chloride hexahydrate (FeCl<sub>3</sub>·6 H<sub>2</sub>O, >99 %) and zinc chloride dihydrate (ZnCl<sub>2</sub>·2 H<sub>2</sub>O, >99 %) from Sigma Aldrich, and ammonia solution (NH<sub>4</sub>OH; 33 %) and *N*-methyl-2-pyrrolidone (NMP) were purchased from Across. All chemicals received were of analytical grade and were used as received, except for aniline monomer, which was distilled twice before use. Double-deionized water was used for electrolyte preparation.

### 2.2. Physico-chemical characterization

For morphological and elemental compositional analysis, scanning electron microscopy (SEM) coupled with energy-dispersive X-rays (EDX) spectroscopy was conducted using a field-emission scanning electron microscope (FESEM, JSM 5910 JEOL). X-ray diffractometry was employed using a diffractometer (Rigaku, having Smart-Lab Studio II software) with a Cu-Kα (λ = 1.54 Å) radiation with 2θ ranging from 10° to 80°, step width of 0.0164°, and a step rate of 1 s<sup>-1</sup>.

Structural characterization of the synthesized polyaniline (PN) and its composites was carried out using a Fourier-transform infrared (FT-IR) spectrometer (IR-Affinity S1, Shimadzu) over a scanning range of 450–4000 cm<sup>-1</sup>, with a resolution of 2 cm<sup>-1</sup>. Additional analyses were performed using a UV-Vis spectrometer (UV-Vis Model 1800, Shimadzu) in the 200–1000 nm range.

### 2.3. Electrochemical characterization

All electrochemical synthesis and analyses were conducted using a Reference 3000 potentiostat/galvanostat (Gamry Instruments). Cyclic voltammetry (CV) measurements were executed in a three-electrode configuration using a gold sheet working electrode (1 cm<sup>2</sup>) – either blank or polymer composite coated – and a gold rod counter electrode, while saturated calomel electrode (SCE, KCl<sub>sat</sub> in H<sub>2</sub>O) as reference. Galvanostatic charge-discharge (GCD) measurements were performed using the same three-electrode assembly. Specific capacitances were determined from CV and GCD curves for each sample using Eqs. (1) and (2) respectively [21].

$$C_s = \int \frac{I \cdot dv}{2m \cdot \nu \cdot \Delta V} \quad (1)$$

$$C_s = \frac{I \cdot t}{m \cdot V} \quad (2)$$

Here,  $\int I \cdot dv$  is the integrated charge of the CV curve (C),  $m$  is the mass (g) of the active material,  $\nu$  is the scan rate (mV s<sup>-1</sup>),  $\Delta V$  is the potential window (V),  $t$  is the discharge time (s), and  $V$  is the IR-drop corrected potential (V).

Additionally, energy density (Wh kg<sup>-1</sup>), power density (W kg<sup>-1</sup>), and coulombic efficiency  $\eta$  (%) were calculated from Eqs. (3), (4), and (5), respectively. [22–24]

$$E = \frac{C_s \cdot (\Delta V)^2}{2} \quad (3)$$

$$P = \frac{3600 \cdot E}{t} \quad (4)$$

$$\eta(\%) = \frac{t_d}{t_c} \cdot 100 \quad (5)$$

Here,  $t_d$  and  $t_c$  are discharge and charge times in seconds (s).

Furthermore, electrochemical impedance spectroscopy (EIS) was employed to investigate charge transfer resistance ( $R_{CT}$ ) at the electrode/electrolyte interface, ions diffusion, and internal resistance ( $R_s$ ), by fixing the excitation amplitude at  $5\text{ mV}_{\text{rms}}$ , within the  $10^5\text{ Hz}$  to  $10\text{ mHz}$  frequency range at an open circuit.

#### 2.4. Synthesis of metal oxide nanoparticles

Co-precipitation was carried out to synthesize different metal oxide nanoparticles.[25] For the synthesis of ZnO and  $\text{Fe}_2\text{O}_3$ ,  $\text{ZnCl}_2 \cdot 2\text{H}_2\text{O}$  (1.36 g, 10.0 mmol, 1.0 eq) and  $\text{FeCl}_3 \cdot 6\text{H}_2\text{O}$  (2.70 g, 9.98 mmol, 1.0 eq) were dissolved in 100 mL distilled water, respectively, and stirred at  $80\text{ }^\circ\text{C}$  for 30 min. The mixture was filtered, and ammonia solution (33 %) was added dropwise until a pH of 10 was set. The nanoparticles precipitated as their respective hydroxides. They were filtered, washed with distilled water and ethanol, and dried at  $120\text{ }^\circ\text{C}$  for 20 min. Then, they were calcined at  $600\text{ }^\circ\text{C}$  for 2 hours with a heating rate of  $10\text{ }^\circ\text{C}/\text{min}$  to obtain ZnO and  $\text{Fe}_2\text{O}_3$  nanoparticles, respectively. The same procedure was used to synthesize  $\text{ZnFe}_2\text{O}_4$  nanoparticles using ZnO and  $\text{Fe}_2\text{O}_3$  in a 1:1 eq. ratio.

#### 2.5. Potentiostatic synthesis of PN hybrid electrodes

A multistep synthesis sequence was used to synthesize the PN composites. An aniline precursor solution was prepared by dispersing aniline (1.0 mL, 10.9 mmol, 1.0 eq) in distilled water. Then,  $\text{H}_2\text{SO}_4$  (5.55 mL, 1 M) and DBSA (0.5 mL, 2.2 mmol, 2.01 eq) were added. The solution was thoroughly mixed, and distilled water was added to a total volume of 100 mL [26,27]. In the case of the PN composite synthesis, the metal oxides (0.1 g) were added to the solution.

Potentiostatic electrodeposition of PN and metal oxide integrated PN composites was carried out using chronoamperometry in a three-electrode setup. Suitable potentials for aniline polymerization, already determined from the LSV technique, i.e.,  $+0.8\text{ V}$  vs. SCE, were applied for 600 s to get a thin PN film, followed by negative potential to achieve ion exchange with the Zn and Fe oxide nanoparticles [28]. For example, a potential of  $-0.6\text{ V}$  was applied vs. SCE to deposit ZnO nanoparticles over 600 s to yield the PNZ.

Similarly, for the deposition of  $\text{Fe}_2\text{O}_3$  and  $\text{ZnFe}_2\text{O}_4$  particles,  $-0.7\text{ V}$  and  $-0.9\text{ V}$  were applied for 600 s to obtain PNF and PNZF. The electrodeposition process was repeated three times to get a fully covered electrode. The composites were thoroughly washed with distilled water and dried with acetone afterward for physico-chemical analysis.

### 3. Results and discussion

#### 3.1. Identification of potentials for the potentiostatic electrodeposition

The key to uniform electrochemical polymerization is identifying suitable reaction conditions, primarily the applied potential. All potentiostatic syntheses and measurements were conducted in sulfuric acid ( $\text{pH} = 1$ ) and at room temperature, to achieve comparable conditions to most chemical synthesis. As substrate or current collector gold sheets were used, as the material is well-suited to analyze PN composites due to its inertness, high stability and high overpotential to the hydrogen evolution and oxygen evolution reaction. Several other substrates were tested, such as stainless steel, lead, silver and copper, but failed in the deposition of lacked stability.

The key for the electrochemical synthesis is controlling the potential at the working electrode. It must be high enough to initiate polymerization but not so high as to trigger over-oxidation or the formation of degradation products [17,29]. Potentials in the range of  $+0.8\text{ V}$  to  $+0.9\text{ V}$  for aniline polymerization led to optimal growth and conversion of conductive polyaniline thin films, whereas potentials above this range caused over-oxidation, as indicated by the reduction in specific capacitance at higher potentials [29]. To facilitate the incorporation of metal

oxide nanoparticles into the polyaniline, the applied potential was reversed to negative potentials. At  $-0.6\text{ V}$  for ZnO,  $-0.7\text{ V}$  for  $\text{Fe}_2\text{O}_3$ , and  $-0.9\text{ V}$  for  $\text{ZnFe}_2\text{O}_4$ , smaller and uniformly distributed nanoparticles formed, leading to a highly porous structure and increased electrochemically active surface area, as seen in SEM analysis (Fig. 1b and Fig. 3). More negative potentials led to nanoparticle aggregation, negatively affecting uniformity and conductivity. This precise control of potential is a key advantage of the potentiostatic method, enabling better morphology and enhanced electrochemical performance compared to traditional methods.

Chronoamperograms depict the non-linear current response during polymer growth (Fig. 2). Initially, a rapid increase in current density was observed for pure PN at  $+0.9\text{ V}$  vs. SCE, lasting about 50 s, due to fast polymerization kinetics of polyaniline [30]. The increase was followed by a decrease in current density over approximately 170 s due to the growth of longer polymer chains and fast consumption of aniline in the diffusion layer, leading to a mass transport limitation. With an increase in the chain length, the polymerization's reaction kinetics decrease, preventing mass transport limitation and resulting in a steady rise in current density until the end of the polymerization [31]. A similar trend was observed during the PN polymerization in the presence of ZnO,  $\text{Fe}_2\text{O}_3$ , and  $\text{ZnFe}_2\text{O}_4$  metal oxide particles [32,33].

#### 3.2. Physico-chemical characterization of the polyaniline composites

The physicochemical material properties of pristine polyaniline (PN) and its composites, PNZ, PNF, and PNZF, are discussed in the following.

For supercapacitors, structural features like porosity and high surface area are directly related to good supercapacitive performance. A high surface area with porous morphology provides more active sites for electrolyte accessibility to facilitate ion transport. The tunable morphology produced by the potentiostatic method, which has a positive effect on the performance of hybrid electrodes, was investigated using SEM analysis.

Fig. 3a, b shows the SEM images of  $\text{Fe}_2\text{O}_3$  and  $\text{ZnFe}_2\text{O}_4$  nanoparticles, which are in the nano range. For pristine PN irregular agglomerated short fibrous growth patterns were observed with an average strand length of  $\sim 0.5\text{ }\mu\text{m}$  and less than 20 nm width (Fig. 3c). Both, PN and PNF exhibit dens nanostructures that are strongly agglomerated with several nanometer-sized particles shown in Fig. 3c, d. Agglomeration, particularly noticeable for PNF, can be attributed to the magnetic properties of the  $\text{Fe}_2\text{O}_3$  nanoparticles incorporated in the polymer

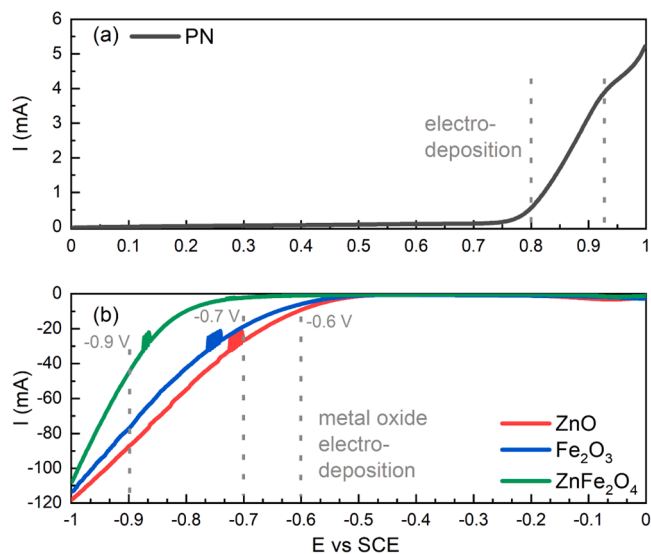


Fig. 1. (a) Linear sweep voltammetry (LSV) of aniline, and (b) ZnO,  $\text{Fe}_2\text{O}_3$ , and  $\text{ZnFe}_2\text{O}_4$  nanoparticles for in situ synthesis of PNZ, PNF, and PNZF composites.

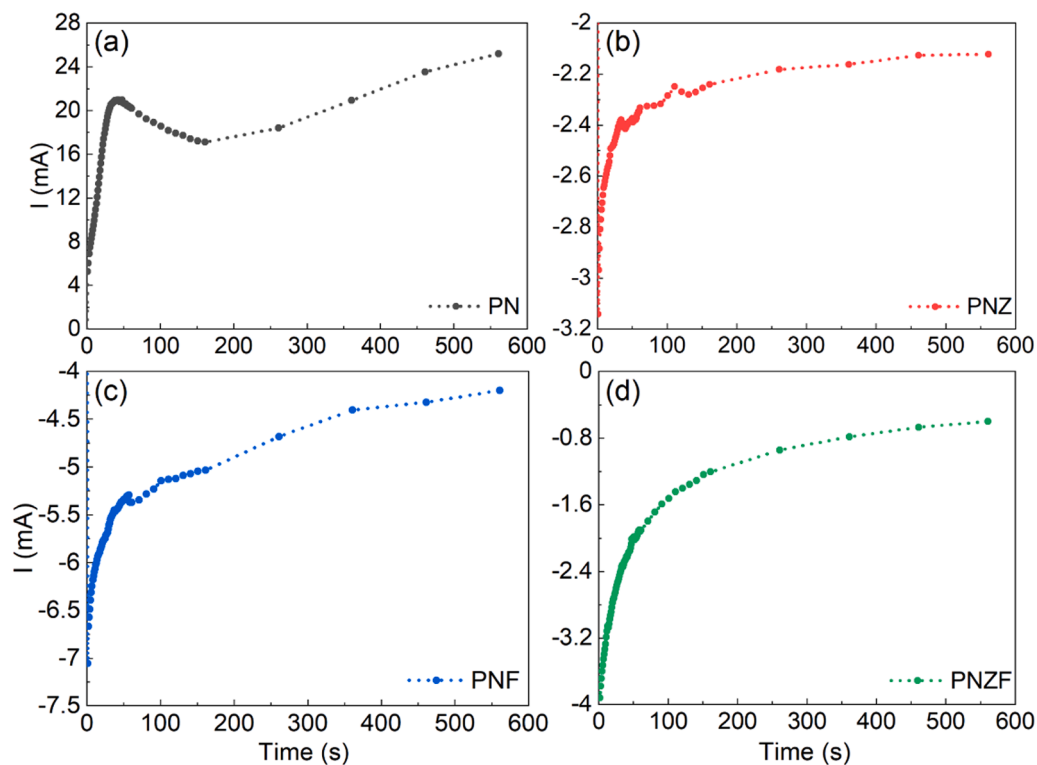


Fig. 2. Current-time response ( $I-t$ ) profiles during synthesis of (a) PN, (b) PNZ, (c) PNF, and (d) PNZF.

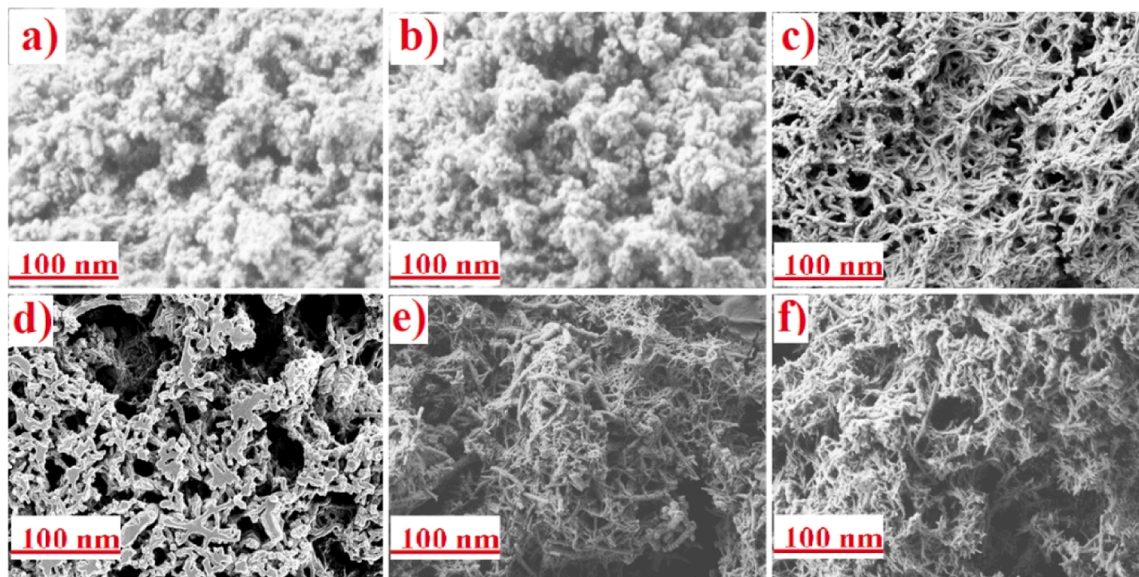


Fig. 3. SEM images of (a)  $\text{Fe}_2\text{O}_3$ , (b)  $\text{ZnFe}_2\text{O}_4$ , (c) PN, (d) PNF, (e) PNZ, and (f) PNZF.

structure [34].

In contrast, PNZ and PNZF show short fibrous growth patterns, with average strand lengths of  $\sim 40\text{--}60$  nm and strand widths between 25 and 30 nm (Fig. 3e, f). The surface is rougher, with tiny nanoparticles of ZnO and  $\text{ZnFe}_2\text{O}_4$ . Further, large vacancies of  $1\text{--}3$   $\mu\text{m}$  in diameter are visible. The open structure of PNZF supports the hypothesis that Zn counteracts the agglomeration effect of iron oxide, as reported in the literature [35].

Patil et al. synthesized the PNFZ composite using a chemical oxidative method with 10 wt% zinc ferrite, producing similar particles but in larger sizes, approximately  $\sim 600$  nm [36]. In contrast, our method demonstrates the production of PNZF with a larger surface area and

higher porosity, validating the viability of the potentiostatic polymerization.

Structural features of PN and its composites with metal oxides were analyzed using X-ray diffraction (XRD), as shown in Fig. 4. The XRD pattern of PN synthesized by cyclic voltammetry and chronoamperometry exhibited a single broadband at  $2\theta = 25.9^\circ$  and  $32.1^\circ$ , indicating its highly amorphous nature (Figs. 4a and 4b). The XRD pattern of ZnO and PNZ showed characteristic peaks at  $2\theta = 32.1^\circ$ ,  $34.7^\circ$ ,  $37.1^\circ$ ,  $47.3^\circ$ ,  $57.7^\circ$ , and  $67.9^\circ$ , consistent with previously reported values (Fig. 4c and d) [28]. The XRD pattern of  $\text{Fe}_2\text{O}_3$  exhibited characteristic peaks at  $2\theta = 24.2^\circ$ ,  $34.0^\circ$ ,  $35.6^\circ$ ,  $42.0^\circ$ ,  $49.7^\circ$ ,  $54.2^\circ$ ,

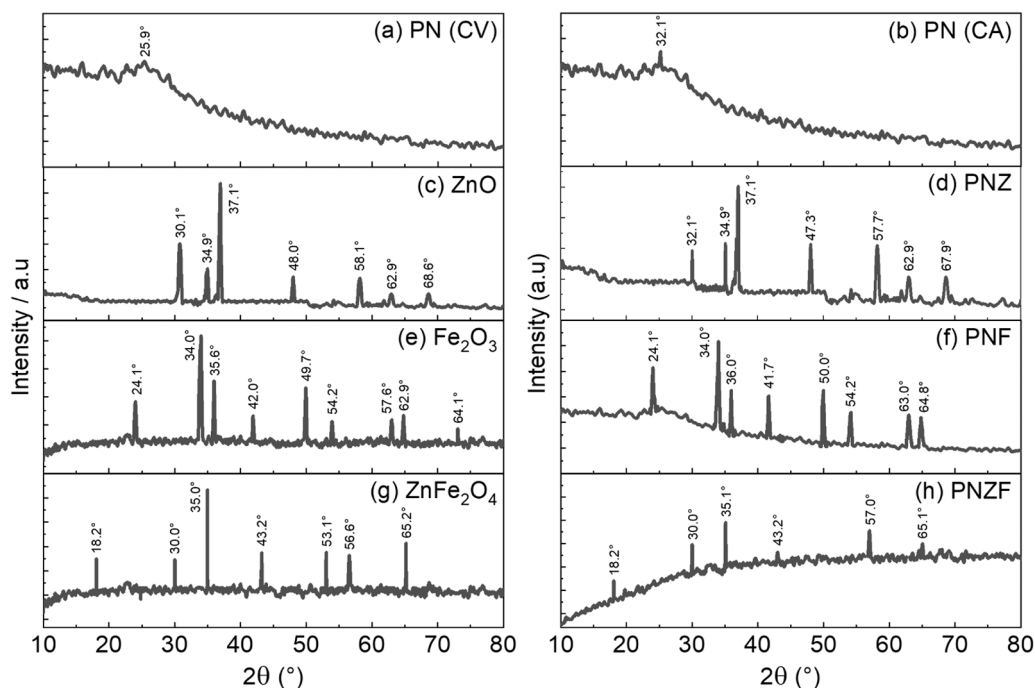


Fig. 4. XRD spectra of (a) PN synthesized by potentiodynamic polymerization (LSV) during parameter identification, (b) PN synthesized by potentiostatic polymerization, (c) ZnO, (d) PNZ, (e) Fe<sub>2</sub>O<sub>3</sub>, (f) PNF, (g) ZnFe<sub>2</sub>O<sub>4</sub>, (h) PNZF.

57.6°, 62.9°, and 64.1°, indicating its crystalline nature without any impurities (Fig. 4e and f) [37,38]. The diffraction peaks of zinc ferrite and PNZF (Figs. 4g and 4h) were observed at positions  $2\theta = 18.2^\circ$ ,  $30.1^\circ$ ,  $35.41^\circ$ ,  $43.1^\circ$ ,  $53.2^\circ$ ,  $56.3^\circ$ , and  $65.2^\circ$ , consistent with the spinel cubic phase due to the presence of hexagonal ZnO and Fe<sub>2</sub>O<sub>3</sub>, forming the bimetallic ZnFe<sub>2</sub>O<sub>4</sub> [39]. The average crystallite size ( $D$ ) was calculated using Scherer's equation (Eq. 6):

$$D = (K \cdot \lambda) / (\beta \cdot \cos \theta) \quad (6)$$

Here is  $K = 0.9$  (Scherer constant),  $\lambda = 0.15406$  nm (wavelength of X-rays),  $\beta$  = full width at half maximum (FWHM) in radians, and  $\theta$  is the peak position on the x-axis.

The peak position and FWHM from XRD data were used to calculate the average crystallite size for ZnFe<sub>2</sub>O<sub>4</sub>, PNZF, Fe<sub>2</sub>O<sub>3</sub>, PNF, ZnO, and PNZ, which were found to be 21.51 nm, 25.34 nm, 29.42 nm, 27.2 nm, 33.19 nm, and 24.7 nm, respectively.

The chemical structure and functional groups of metal oxides, PN, and its composites were investigated by FTIR analyses. The FTIR spectra of pure PN and its composites show clear characteristic peaks (Table 1). For example, the peak at  $3260 \text{ cm}^{-1}$  corresponds to the N-H bond stretching vibrations in the PN polymer chain (Fig. 5a) [40]. In addition, a notable and relatively intense peak at  $1530 \text{ cm}^{-1}$  indicates the C=C stretching of the benzoid ring. The persistence of this peak in the composites confirms the retention of polymer composition even after potentiostatic deposition of metal oxides. The EDX pattern shown in Figure S1 also affirms that the electrochemical incorporation of various

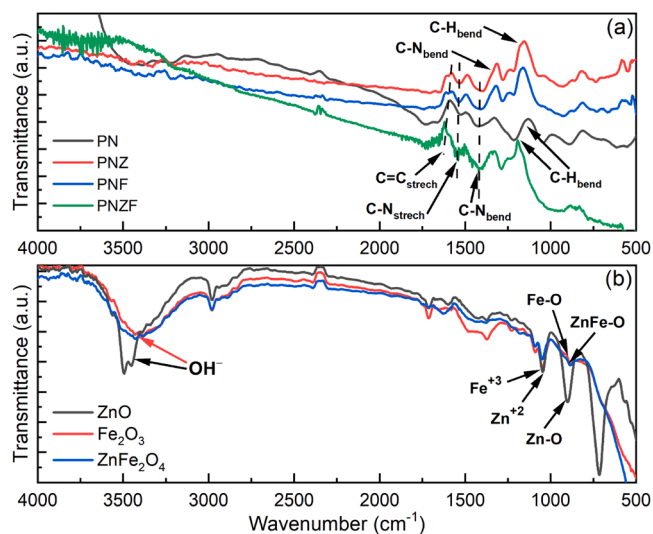


Fig. 5. FT-IR spectra of (a) PN and its composites, (b) ZnO, Fe<sub>2</sub>O<sub>3</sub> and ZnFe<sub>2</sub>O<sub>4</sub>.

Table 1  
Position of FTIR vibrations observed for the PN and PN composites.

PN (cm <sup>-1</sup> )	PNZ (cm <sup>-1</sup> )	PNF (cm <sup>-1</sup> )	PNZF (cm <sup>-1</sup> )	Peak assignments
1105	1134	1138	1153	CH bending
1303	1308	1307	1370	-N=Quinoid=N-
1402	1402	1403	1405	CN bending
1570	1570	1571	1579	CN stretching
1581	1577	1574	1580	Benzenic quinoinic nitrogen
1608	1609	1610	1619	C=C stretching

metal oxide particles into the polymers does not affect the polymer composition.[41] The peak at  $1490 \text{ cm}^{-1}$  is assigned to C-N stretching vibration, which is more pronounced in the composites than pristine PN, indicating the attachment of metal oxides. The characteristic bands in the  $1142\text{--}1154 \text{ cm}^{-1}$  range are assigned to the C-H bending vibration in the plane of the aromatic benzoid/quinoid rings, which also explains the delocalization of the pi electrons [42]. The FTIR spectra of the metal oxides (see Fig. 5b) explain the structural features of corresponding metal oxides. The bands at  $720$ ,  $950$ , and  $1060 \text{ cm}^{-1}$  can be assigned to ZnO, Fe<sub>2</sub>O<sub>3</sub>, and ZnFe<sub>2</sub>O<sub>4</sub>, respectively. A broad band at  $3500 \text{ cm}^{-1}$ , present in the FTIR spectra of all metal oxides, is due to OH stretching. This band illustrates the porous nature of the metal oxides, which contain moisture in the pores of the metal oxides [43]. This peak is more pronounced and broader in the spectrum of ZnO, indicating a higher water content than other metal oxides.

Optical characterization of metal oxides, PN, and the PN composites was done to gain insights into their doping level and charge transport during electronic excitation. Therefore, all the samples were dissolved in appropriate amounts of NMP, and UV-vis spectra were recorded in the 200–800 nm range. The obtained spectra for metal oxides and PN composites are shown in Fig. 6a and Fig. 6b, respectively.

The UV-vis spectra of PN and PN composites reveal three characteristic peaks. The first peak in the 720–800 nm range is attributed to the creation of excitons that cause the bipolaronic transition [12]. The bipolaronic transition in PNZF was observed at 750 nm, while for PNZ and PNF, it was observed at 680 nm and 800 nm, respectively. The second peak in the 380–430 nm range represents the polaron transition of quinoid rings in PN and composites [44]. The relatively higher intensity absorbance peaks observed in the 280–300 nm range represent the  $\pi$ - $\pi^*$  transition of the aromatic/benzoid rings of composites and pure PN [45]. Specifically, for PNZF, this peak was observed at 280 nm, while for PNF and PNZ, it was observed at 300 nm and 290 nm, respectively.

On the other hand, the UV-Vis spectra of metal oxides showed a single and characteristic absorption peak in the range of 270–320 nm. The absence of extra peaks implies the purity and well-crystalline nature of the metal oxides [46]. This single prominent and characteristic absorption peak was observed at 270 nm for ZnO, 320 nm for Fe<sub>2</sub>O<sub>3</sub>, and 380 nm for ZnFe<sub>2</sub>O<sub>4</sub>. [47] The shifting of peak position is related to bathochromic shift, which was a reason for selecting bimetal oxides to synthesize an imminent hybrid electrode for future supercapacitors.

### 3.3. Electrochemical characterization of the polyaniline composites

To investigate that the PN composites are suitable as electrode material for supercapacitors, the electrochemical properties were investigated by cyclic voltammetry (CV), galvanostatic charge-discharge (GCD), and electrochemical impedance spectroscopy (EIS).

Since the cyclic voltammetry of PANI composites has already been described in detail in the literature, only the general behavior is presented here. Fig. 7 shows PN, PNZ, PNF, and PNZF CVs between potentials of  $-0.2$  V and  $0.9$  V (vs. SCE, KCl<sub>sat.</sub> in H<sub>2</sub>O) with different scan rates. All electrochemical measurements were carried out in  $1$  M H<sub>2</sub>SO<sub>4</sub> electrolyte solution. Fig. 7a depicts the cyclic voltammogram of polyaniline (PN), revealing three distinct redox transitions. The first oxidation peak at  $0.17$  V corresponds to the conversion from leucoemeraldine to emeraldine while the 3<sup>rd</sup> oxidation peak at  $0.77$  V corresponds to its further oxidation to pernigraniline. The middle peak at  $0.45$  V can be attributed to smaller polymer chains undergoing additional chain growth, ion doping/de-doping processes, or the degradation products

present in the film. The oxidation peaks are accompanied by corresponding reduction peaks on the reverse scan at  $-0.03$ ,  $0.64$ , and  $0.37$  V, respectively.

For PNZ, PNF, and PNZF, analogous electrochemical behaviors were observed in the CVs (Fig. 7b-d). These composites also display three distinct redox transitions visible at low scan rates. However, at higher scan rates, the peaks merge due to the increased current, resulting in near-rectangular CV shapes attributed to the heightened double-layer capacitance. Furthermore, an upward shift in the potential of the redox peaks at faster scan rates suggests hindered charge transfer.

When comparing the cyclic voltammograms (CVs) of polyaniline (PN) and its composites, it is evident that PNZF has the highest redox activity (Fig. 8a). The redox transition of the PNZF composite, from its emeraldine form to the fully oxidized pernigraniline state, is observed at  $0.81$  V with a corresponding reduction peak at  $0.64$  V. These peaks show the highest current density compared to other samples. This is due to the incorporation of ZnFe<sub>2</sub>O<sub>4</sub> that increases the redox behavior of polyaniline. Similarly, the reverse scan of PNZF at a scan rate of  $5$  mV s<sup>-1</sup> as indicated in Fig. 8a reveals two prominent peaks, further supporting the presence of Zn and Fe ions which contribute to the energy storage mechanism. PNZ and PNF exhibit a similar trend, contrasting with pristine PN [48]. From the comparative CVs, the highest specific capacitance of  $816$  F g<sup>-1</sup> was obtained for PNZF at a scan rate of  $5$  mV s<sup>-1</sup>. For PNF, PNZ, and PN, lower specific capacitances of  $597$ ,  $359$ , and  $331$  F g<sup>-1</sup> were obtained, respectively. Thus, incorporating ZnFe<sub>2</sub>O<sub>4</sub> significantly increased charge storage capability compared to the other electrode materials. As the scan rate increases, all composites' specific capacitances drop steadily. This trend occurs due to the slow mass transport of electrolyte ions inside the porous active material. Consequently, the charge storage capability is lower (Fig. 8b).

The current dependence on scan rate was analyzed using Eq. (7) to investigate further the charge storage mechanism occurring at the electrode-electrolyte interface [24,49].

$$\log I = \log a + b \log v \quad (7)$$

In this equation,  $b$  represents the slope directly associated with the charge storage mechanism. For instance, a value of "b" equal to  $0.5$  suggests a diffusion-controlled process, while a value higher than  $0.5$  indicates a surface-controlled process. Among the different electrode materials investigated, PNZF exhibited the highest values:  $0.81$  for oxidation and  $0.73$  for reduction (Figure S2), suggesting a surface-controlled process. However, the impact of mass transport by ion diffusion still contributes to the overall performance at high scan rates [24].

The surface-controlled charge storage mechanism was correlated with the electrochemically active surface area (ECSA) by comparing the ECSA of pristine PN and PN hybrid materials at a scan rate of  $20$  mV/s using Eq. (8) [50] (see also Figure S3).

$$A_o/A = (i_1 v_2 / i_2 v_1)^{\alpha-1/2} \quad (8)$$

Here  $A_o$  is the ECSA of pristine PN,  $A$  is the ECSA of the hybrid electrodes,  $i_2$  and  $i_1$  are the anodic peak currents, and  $v_2$  and  $v_1$  are the scan rates of pristine PN and hybrid electrodes, respectively.  $\alpha$  is the fractal dimension and is greater than  $2$  for metal oxides; when set at  $2$  for this analysis, the ECSA was found to be  $4.6$  times higher for PNZF than for PN, while for PNZ and PNF, it was  $4.01$  and  $1.58$  times higher, respectively. The increase in ECSA of hybrid electrodes compared to PN electrodes implies efficient potentiostatic integration of metal oxide nanoparticles, which enhances the porosity and ECSA of the resulting hybrid electrodes. The comparative increase in ECSA observed for PNF compared to PNZF is attributed to large voids, as revealed by its SEM images. However, aggregation was still noted due to the high magnetic nature of Fe<sub>2</sub>O<sub>3</sub> nanoparticles [51].

Moreover, the cycle stability of PN and its composites was investigated at  $30$  Ag<sup>-1</sup> for  $4000$  consecutive GCD cycles within the potential

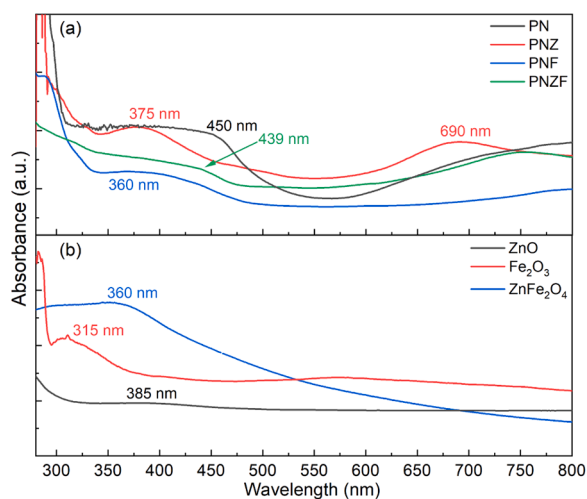


Fig. 6. UV/Vis spectra of (a) PN and its composites and (b) ZnO, Fe<sub>2</sub>O<sub>3</sub>, and ZnFe<sub>2</sub>O<sub>4</sub>.

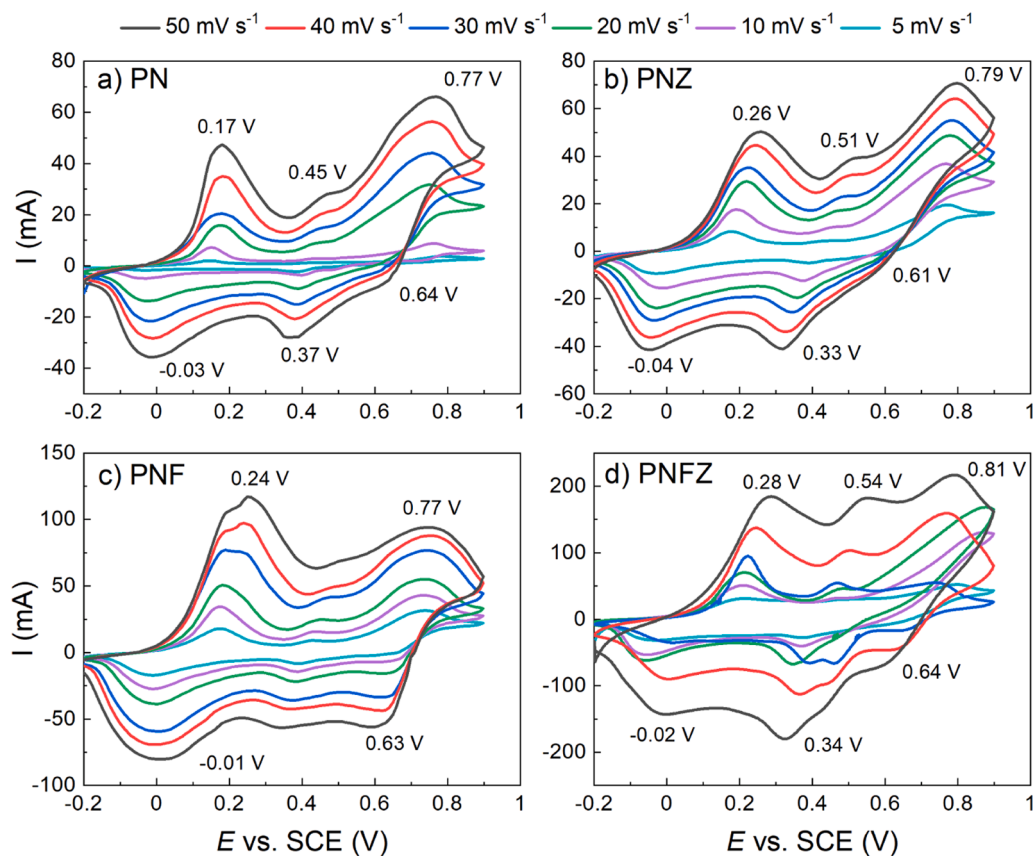


Fig. 7. Cyclic voltammograms of (a) PN, (b) PNZ, (c) PNF, and (d) PNZF at different scan rates. Potentials are referred to as SCE ( $\text{KCl}_{\text{sat}}$  in  $\text{H}_2\text{O}$ ).

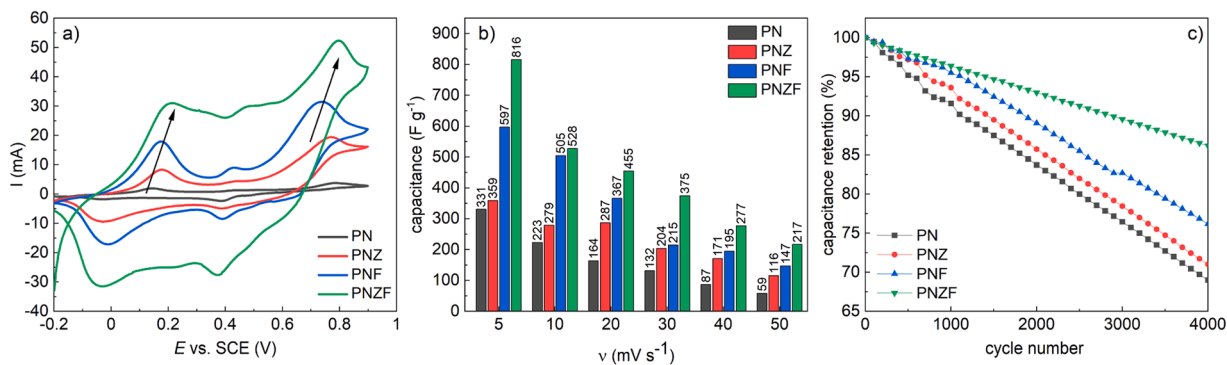


Fig. 8. Comparison of PN and its composites for (a) CV measurements at a scan rate of 5  $\text{mV s}^{-1}$ , (b) the calculated specific capacitances of PN, PNZ, PNF, and PNZF for different scan rates, (c) the calculated capacitance retentions for 4000 cycles at 30  $\text{mV s}^{-1}$ .

range of 0–1.1 V. As illustrated in Fig. 8c, all four polymers exhibit a linear decrease in capacitance retention over the entire cycling duration. PN and PNZ demonstrate comparable and relatively low cycle stability, dropping below 70 % capacitance retention after 4000 cycles. Similarly, PNF follows a similar trend with a capacitance retention of approximately 80 % over the cycling experiment. Notably, the highest capacitance retention is observed for PNZF, reaching 90 % throughout the entire testing period. The linear decrease in capacitance retention suggests a consistent degradation mechanism persisting throughout the cycle test, with no additional processes occurring in the later stages that alter the rate of performance loss.

Fig. 9 shows the GCD profiles of PN and its composites at different current densities between 0.5  $\text{F g}^{-1}$  to 10  $\text{F g}^{-1}$ . The asymmetric and distorted triangular shape in the potential range from 0 V to 1.1 V originates from the pseudocapacitive behavior of the materials. It is

incredibly dominant for PNF and PNZF, thus underscoring their high pseudocapacitive nature compared to PN and PNZ samples (Fig. 9a-d). Notably, the charge-discharge duration of PNZF surpassed that of the other samples, suggesting the positive contribution of  $\text{ZnFe}_2\text{O}_4$  doping to the polymer structure. The synergistic interaction between the  $\text{ZnFe}_2\text{O}_4$ -dopant and the polymer network increased electrical double-layer capacitance, additionally to the pseudo-capacitance stemming from redox reactions at the electrode interface.

Furthermore, in the case of PN, PNZ, and PNF, a noticeable instantaneous voltage drop occurs when the supercapacitor changes from charging to discharging. This drop results from the cumulative ohmic resistance of the electrodes, electrolyte, and contact resistances within the electrode structure. Consequently, the IR drop reduces the total usable voltage window ( $\Delta V$ ), contributing to these three materials' lower charging and discharging times. For PNZF, the IR drop is significantly

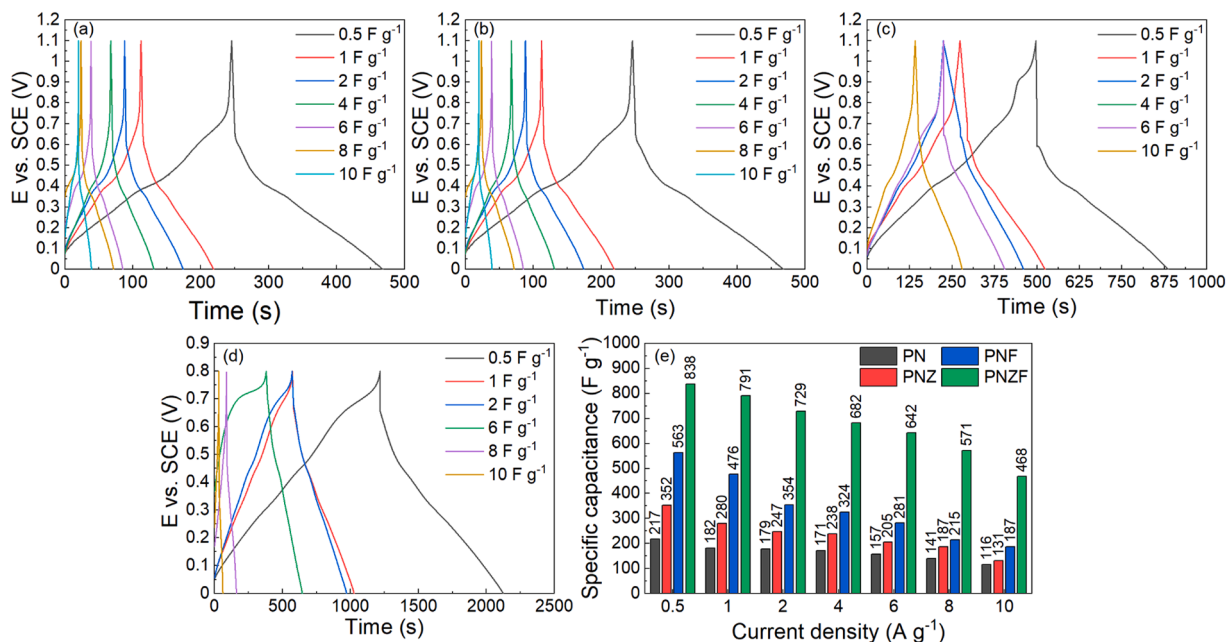


**Fig. 9.** GCD experiments at different current densities of (a) PN, (b) PNZ, (c) PNF, and (d) PNZF. (e) Comparison of the specific capacitances of PN and its composites at different current densities.

lower; thus, the charge and discharge time are higher.

Consequently, the comparison reveals significantly lower specific capacitances for PN, PNZ, and PNF of 476, 280, and 182 F g<sup>-1</sup>, respectively, at a current density of 1 A g<sup>-1</sup>. In contrast, PNZF exhibits the highest specific capacitance of 791.3 F g<sup>-1</sup> at the same current density. These findings are consistent with those obtained from the CV analysis. Moreover, the decrease in specific capacitances with increasing current densities across the various electrodes suggests that the processes are predominantly surface-controlled and exhibit only mass transport limitations at high current densities, as indicated by the CV results [11].

Table 2 compares various polyaniline composite electrode materials in a three-electrode setup. The analysis of PNZF reveals comparable charge storage capabilities to those incorporating cobalt-iron oxide and nickel-iron oxides; however, it stands out due to its non-toxic dopant. Consistent with PN composites, PNZF exhibits a notably high power density of 1058.4 W kg<sup>-1</sup> alongside a moderate energy density of 136.4 Wh kg<sup>-1</sup> at 1.0 A g<sup>-1</sup>, making it suitable for high-power applications.

### 3.4. Analysis of PN and its composites in a symmetrical supercapacitor

For realistic performance analysis of PN, PNZ, PNF, and PNZF, they were assembled in a symmetrical supercapacitor and investigated by GCD and EIS in a two-electrode setup. The symmetrical setup results in similarly shaped charge-discharge curves that became more rectangular.

**Table 2**  
Comparison of various PN/metal oxide electrodes for supercapacitors.

Electrode material	Method of synthesis	Capacitance (F g <sup>-1</sup> ) at 1 A g <sup>-1</sup>	Energy density (Wh kg <sup>-1</sup> )	Power density (W kg <sup>-1</sup> )	Capacitance Retention (%)	References
PN/GO/ ZnFe <sub>2</sub> O <sub>4</sub>	Hydrothermal	594	45.2	302.7	82	[52]
PN/Fe <sub>2</sub> O <sub>3</sub> /rGO	Chemical oxidative polymerization	283.4	47.4	550	78	[53]
PN@Fe-Ni co-doped Co <sub>3</sub> O <sub>4</sub>	In-situ oxidative polymerization	1171	144	—	84	[8]
PN/NiFe <sub>2</sub> O <sub>4</sub> / rGO	In-situ oxidative polymerization	1134.2	19.3	610	76.5	[11]
PN/CoFe <sub>2</sub> O <sub>4</sub> / GO	Chemical oxidative polymerization	1123	240	2680	98.2	[54]
PNZF	Potentiostatic electrochemical polymerization	791.3	136.4	1058.4	90	this work

Their specific capacitances were calculated from the discharge curves measured at 1 A g<sup>-1</sup>, and the respective energy, power density, and coulombic efficiency were determined (see Table 3).

PN exhibits moderate charge storage capabilities with a specific capacitance of 181.3 F g<sup>-1</sup>. It demonstrates a relatively high power density at 1058.4 W kg<sup>-1</sup>, albeit with a moderate energy density of 31.3 Wh kg<sup>-1</sup>. Despite this, PN maintains a high Coulombic efficiency of 130.3%. In contrast, PNZ exhibits slightly improved charge storage properties with a higher specific capacitance of 280.6 F g<sup>-1</sup>. However, its power and energy density are comparatively lower at 774.0 W kg<sup>-1</sup> and 25.9 Wh kg<sup>-1</sup>, respectively. The low specific capacitance for PNZ contradicts the results from the three-electrode measurements. The negative polarization of the respective counter electrode in the two-electrode setup may cause losses during the GCD cycles, leading to performance loss.

Additionally, PNZ, like PN, showed a higher coulombic efficiency of 123.9%. A coulombic efficiency higher than 100% indicates an irreversible process occurs during the GCD experiment. This is consistent with the cycle stability experiments with three electrodes, in which PN and PNZ showed the lowest capacity retention over 4000 cycles and, thus, the fastest degradation.

In contrast, PNF demonstrates superior charge storage capabilities compared to PN and PNZ, with a significantly higher specific capacitance of 475.9 F g<sup>-1</sup> and a good energy and power density of 65.1 Wh kg<sup>-1</sup> and 941.4 W kg<sup>-1</sup>, respectively. PNF maintains a high Coulombic efficiency of 90.5%. Amongst the different samples, PNZF

**Table 3**Specific capacitances, energy densities, power densities, and coulombic efficiencies for PN and its composites at 1.0 A g<sup>-1</sup>.

Sample	Charge time (s)	Discharge time (s)	Discharge potential (V)	Specific capacitance (F g <sup>-1</sup> )	Energy density (Wh kg <sup>-1</sup> )	Power density (W kg <sup>-1</sup> )	Coulombic efficiency (%)
PN	81.8	106.6	0.59	181.3	31.3	1058.4	130.3
PNZ	97.4	120.7	0.43	280.6	25.9	774.0	123.9
PNF	275.1	248.9	0.52	475.9	65.1	941.4	90.5
PNZF	564.6	464.1	0.59	791.3	136.4	1058.4	82.2

stands out again with the notably highest specific capacitance of 791.3 F g<sup>-1</sup>. Therefore, the energy and power density were 136.4 Wh kg<sup>-1</sup> and 1058.4 W kg<sup>-1</sup>, respectively, and a coulombic efficiency of 82.2 %. The decrease in coulombic efficiency arises from a prolonged duration for the complete charge-discharge sequence. However, the results show that doping PN with ZnFe<sub>2</sub>O<sub>4</sub> produces excellent performance and energy storage properties suitable for high-power applications.

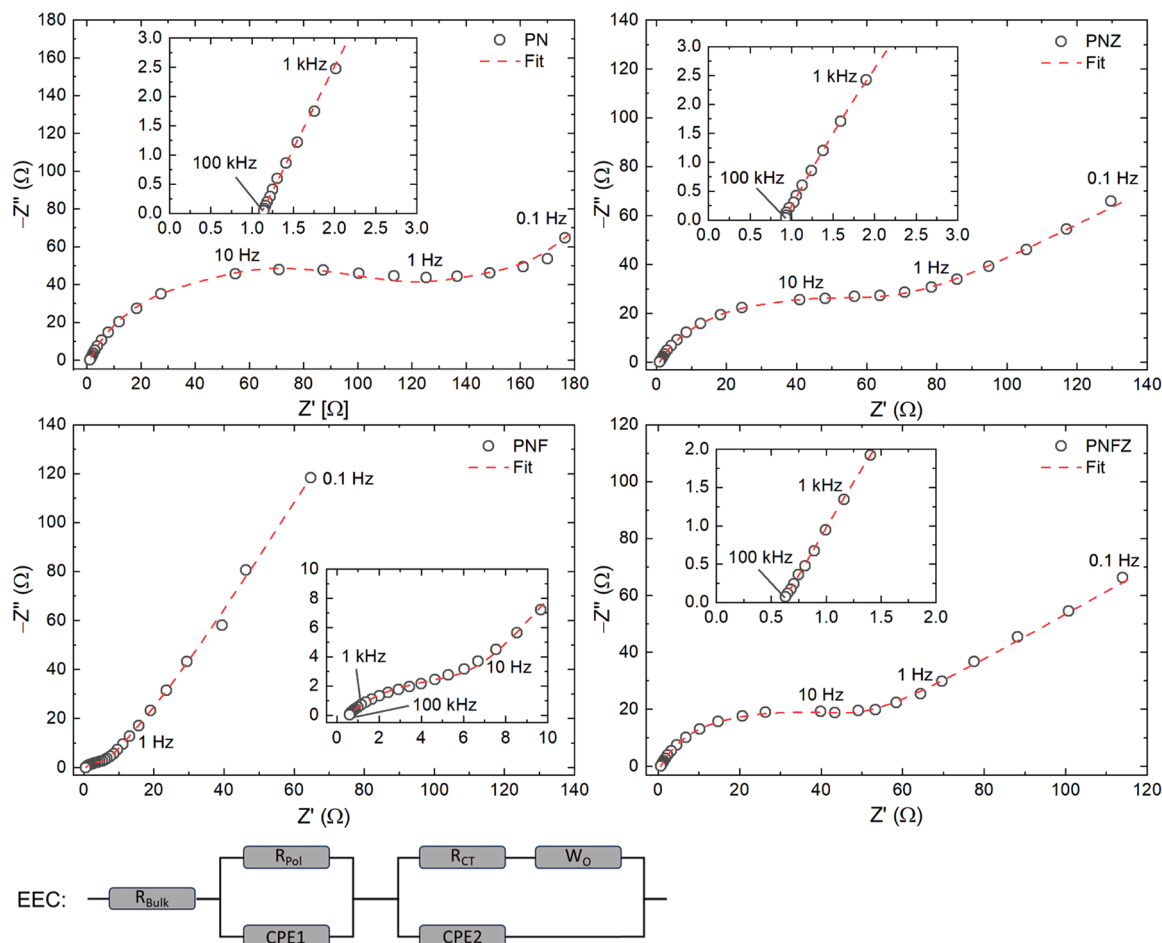
The performance of electrochemical devices involves analyzing various types of losses, including charge transport losses, charge transfer losses due to electrochemical reactions, and losses attributed to reactant diffusion. Electrochemical impedance spectroscopy enables the characterization of these processes individually by separating them by their respective time constants, thus showing their contributions to the total loss. Fig. 10 illustrates the Nyquist plots obtained from measurements conducted on PN and PN composite-coated electrodes at OCP.

The spectra can be divided into three distinct regions: (1) the high-frequency region (> 1 kHz) is attributed to the bulk resistance, comprising the charge transport resistance stemming from the current

collector, wiring, and both electrical and ionic transport through the electrode and electrolyte; (2) a broad and open semi-circle observed in the mid-frequency range (1 kHz to 5 Hz), attributed to the electrode interfaces' double layers, ion transport barriers in the porous electrode channels, and charge transfer processes; [55–57] and (3) a monotonically increasing slope observed at frequencies below 5 Hz to 0.1 Hz, typically associated with ion diffusion within the active material and other slower diffusion processes [58].

Through this analysis, the intricate interplay between these fundamental processes can be identified, providing valuable insights into the loss mechanisms that determine the electrochemical performance of supercapacitors.

The analysis of EIS parameters was done using a simplified electrical equivalent circuit (EEC). This EEC comprises several elements: a bulk resistance ( $R_{\text{Bulk}}$ , > 1 kHz) in series with a polarization resistance ( $R_{\text{pol}}$ ) that is in parallel arrangement with a constant phase element (CPE, 1 kHz – 100 Hz) which describes the increased resistance to the current flow caused by the electrochemical reaction of the active PN composite in the electrical double layer. It is coupled in series with a charge

**Fig. 10.** EIS spectra of PN, PNZ, PNF, and PNZF. The EEC for fitting the spectra is shown below.

transfer resistance ( $R_{CT}$ ) in parallel with another CPE element to fit the pseudocapacitive part of charge transfer (100 kHz – 1 Hz), and an open Warburg element ( $W_o$ , >1 Hz) to model ion transport within the polymer particles.

For all four electrode materials, low bulk resistances ranging from 0.50  $\Omega$  to 1.11  $\Omega$  were observed, underscoring the high conductivity of both the electrode material and the remaining components of the supercapacitor. In the case of PN and PNZ, notably high polarization resistances of 130.6  $\Omega$  and 74.0  $\Omega$  were obtained in the frequency range of 1 kHz to 100 Hz, likely stemming from irreversible loss processes at the electrode/electrolyte interface, such as chain degradation, contributing to their lower Coulombic efficiency. Conversely, PNF and PNZF exhibited lower polarization resistances of 6.45  $\Omega$  and 34.7  $\Omega$ , respectively.

Furthermore, high charge transfer resistances were observed for PN (109.4  $\Omega$ ), while PNZ and PNF showed intermediate values of 44.2  $\Omega$  and 51.5  $\Omega$ , respectively. This indicates kinetic limitations during the electrochemical redox reaction of the polymer for these three cases. In contrast, PNZF demonstrated a significantly lower charge transfer resistance of 25.0  $\Omega$ , suggesting higher efficiency in charge transfer and thereby translating into superior charge storage capability [59]. Additionally, at the low-frequency range, an almost ideal Warburg diffusion behavior was observed across all cases. This finding suggests minimal mass transport influence attributed to slow ion diffusion, indicating a predominantly surface-controlled charge storage mechanism for all materials [60].

These insights highlight the intricate interplay between different resistance components and their impact on the electrochemical performance of the supercapacitor electrodes.

#### 4. Conclusions

In summary, we have employed an efficient potentiostatic method, utilizing a pre-determined optimal working potential to synthesize pristine PN and metal oxides-integrated hybrid electrodes: PNZ, PNF, and PNZF, intended for charge storage in symmetric supercapacitors. SEM analysis confirmed the porous surface morphologies of the hybrid electrodes and irregular, agglomerated short fibrous growth patterns of pristine PN and other PN hybrid electrodes; CV and EIS analysis confirmed the surface-controlled charge storage mechanism that synergizes with the high electrochemical active surface area. Among these, PNZF demonstrated the highest energy storage performance, attributed to the effective potentiostatic integration of spinal zinc-ferrite nanoparticles. The superior energy storage performance of PNZF with specific capacitances of 816 F g<sup>-1</sup> and 791.3 F g<sup>-1</sup> at 5 mVs<sup>-1</sup> scan rate and 1.0 A g<sup>-1</sup> current density is accredited to its pseudocapacitive nature and efficient charge transfer processes. Analysis of GCD profiles in two- and three-electrode setups confirms an energy density of 136.4 Wh kg<sup>-1</sup> and a power density of 1058.4 W kg<sup>-1</sup>, making PNZF a suitable electrode material for high-power charge storage applications. EIS measurements revealed the intricate interplay between different process losses, proving the surface-controlled charge storage mechanism. Moreover, the PNZF exhibited the lowest charge transfer resistance of 25.0  $\Omega$  and 34.7  $\Omega$  polarization resistance, with an ideal Warburg diffusion behavior at low-frequency regions. Furthermore, PNZF showed the highest capacitance retention of ~90 % over 4000 cycles with 82.2 % coulombic efficiency.

Overall, our study demonstrates the promising potential of PN composites, particularly PNZF, as electrode materials for high-performance supercapacitors, offering insights into their structural, optical, and electrochemical properties for future energy storage applications.

#### CRediT authorship contribution statement

**Philipp Röse:** Writing – review & editing, Visualization,

Supervision, Resources, Project administration, Methodology, Funding acquisition, Formal analysis, Data curation. **Anwar ul Haq Ali Shah:** Writing – review & editing, Supervision, Resources, Project administration, Methodology, Funding acquisition, Conceptualization. **Salma Bilal:** Writing – review & editing, Supervision, Resources, Methodology. **Imran Khan:** Writing – original draft, Visualization, Investigation, Formal analysis, Data curation.

#### Declaration of Competing Interest

The authors declare the following financial interests/personal relationships which may be considered as potential competing interests: Anwar ul Haq Ali Shah reports financial support was provided by Higher Education Commission Pakistan. If there are other authors, they declare that they have no known competing financial interests or personal relationships that could have appeared to influence the work reported in this paper

#### Acknowledgements

The authors are thankful to the Higher Education Commission Pakistan for providing funds to establish the Electrochemistry lab at the Institute of Chemical Sciences, University of Peshawar, under NRP project # 20–3111. The APC is funded by the KIT Publication Fund of Karlsruhe Institute of Technology, Germany.

#### Sample avail-ability

Samples of the compounds, i.e., PN, PNZ, PNF, and PNZF, are available from the corresponding authors upon request.

#### Supporting Information

The supporting information includes EDX spectra (Figure S1), and results from the electrochemical analysis of the energy storage mechanism (Figure S2).

#### Appendix A. Supporting information

Supplementary data associated with this article can be found in the online version at [doi:10.1016/j.synthmet.2024.117784](https://doi.org/10.1016/j.synthmet.2024.117784).

#### Data availability

A link to KITOpen Repository is shared in the document.

#### References

- [1] J. Ji, S. Park, J.H. Choi, ACS Omega 8 (2023) 16833–16841.
- [2] M. Horn, J. MacLeod, M. Liu, J. Webb, N. Motta, Econ. Anal. Policy 61 (2019) 93–103.
- [3] M.E. Şahin, F. Blaabjerg, A. Sangwongwanich, Energies 15 (2022) 674.
- [4] R. Wang, X. Li, Z. Nie, Y. Zhao, H. Wang, J. Energy Storage 38 (2021) 102479.
- [5] P. Veerakumar, A. Sangili, S. Manavalan, P. Thanasekaran, K.-C. Lin, Ind. Eng. Chem. Res. 59 (2020) 6347–6374.
- [6] P. Naskar, A. Maiti, P. Chakraborty, D. Kundu, B. Biswas, A. Banerjee, J. Mater. Chem. A 9 (2021) 1970–2017.
- [7] K.P. Gautam, D. Acharya, I. Bhatta, V. Subedi, M. Das, S. Neupane, J. Kunwar, K. Chhetri, A.P. Yadav, Inorganics 10 (2022) 86.
- [8] M. Usman, M. Adnan, M.T. Ahsan, S. Javed, M.S. Butt, M.A. Akram, ACS Omega 6 (2021) 1190–1196.
- [9] S. Vargheese, G. Dhakal, R.S. Kumar, R.T.R. Kumar, J.-J. Shim, Y. Haldorai, J. Energy Storage 71 (2023) 108145.
- [10] F. Azimov, J. Kim, S.M. Choi, H.M. Jung, Nanomaterials 11 (2021) 1557.
- [11] S. Sardana, K. Aggarwal, S. Malik, A. Saini, S. Dahiya, R. Punia, A. Maan, K. Singh, A. Ohlan, Electrochim. Acta 434 (2022) 141324.
- [12] S.S. Shah, M.A. Aziz, A.-R. Al-Betar, W. Mahfoz, Arab. J. Chem. 15 (2022) 104058.
- [13] W. Mahfoz, H.T. Das, S.S. Shah, M. Sanhoob, A. Anjum, A.R. Al-Betar, M.A. Aziz, Chem. Asian J. 18 (2023) e202201223.
- [14] S. Khameneh Asl, M. Maghsoudi, F. Gorbani, J. Ult. Grain. Nanostruc. Mat. 54 (2021) 40–50.

- [15] U. Ghimire, R. Kandel, S.W. Ko, J.R. Adhikari, C.S. Kim, C.H. Park, *Int. J. Bio. Macromol.* 264 (2024) 130608.
- [16] M.A. Sayeed, A.P. O'Mullane, *ChemPhysChem* 20 (2019) 3112–3119.
- [17] E. Kim, N. Kang, J.J. Moon, M. Choi, *Bull. Korean Chem. Soc.* 37 (2016) 1445–1452.
- [18] P. Agale, V. Salve, K. Patil, S. Mardikar, S. Uke, S. Patange, P. More, *Ceram. Ing.* 15 (2023) 27003.
- [19] G. Singh, Y. Kumar, S. Husain, *Energy Storage* 6 (2024) e525.
- [20] A. Soam, 'Application of Ferrites as Electrodes for Supercapacitor', *Ferrites - Synthesis and Applications*, IntechOpen, Nov. 17, 2021, <https://doi.org/10.5772/intechopen.99381>.
- [21] S. Sharma, P. Chand, *Res. Chem.* (2023) 100885.
- [22] A. Chonat, S. Palatty, *Energy Fuels* 34 (2020) 10148–10159.
- [23] X. Lu, H. Yang, Z. Bo, B. Gong, M. Cao, X. Chen, E. Wu, J. Yan, K. Cen, K. Ostrikov, *Energies* 15 (2022) 1191.
- [24] H. Humayun, B. Begum, S. Bilal, A.U.H.A. Shah, P. Röse, *Nanomaterials* 13 (2023) 618.
- [25] S. Slimani, C. Meneghini, M. Abdolrahimi, A. Talone, J.P.M. Murillo, G. Barucca, N. Yaacoub, P. Imperatori, E. Illés, M. Smari, *Appl. Sci.* 11 (2021) 5433.
- [26] M.M. Gvozdenović, B.Z. Jugović, J.S. Stevanović, T.L. Trišović, B.N. Grgur, *Electropolymers* 2011 (2011) 77–96.
- [27] A. Sayah, F. Habelhames, A. Bahloul, A. Boudjadi, *J. Mater. Sci.: Mater. Electron.* 32 (2021) 10692–10701.
- [28] B. Zhao, H.-W. Becker, S. Gutsch, *Nanomaterials* 13 (2023) 2088.
- [29] C.P. Zimmermann, G.M. Kranz, J.P. Eckert, L. Fadani, M. Zanetti, J.M.M. Mello, P. R. Innocente, G.L. Colpani, M.A. Fiori, C.H. Scillacchio, *Mat. Res.* 26 (2023) e20220609.
- [30] J. Quílez-Bermejo, E. Morallón, D. Cazorla-Amorós, *Polymers* 12 (2020) 2382.
- [31] A. Al-Owais, I. El-Hallag, *Polym. Bull.* 76 (2019) 4571–4584.
- [32] W. Huang, J. Li, Y. Xu, *Materials* 11 (2018) 716.
- [33] N. Saurakhiya, S.K. Sharma, R. Kumar, A. Sharma, *Ind. Eng. Chem. Res.* 53 (2014) 18884–18890.
- [34] M. Bustamante-Torres, D. Romero-Fierro, J. Estrella-Núñez, B. Arcentales-Vera, E. Chichande-Proano, E. Bucio, *Polymers* 14 (2022) 752.
- [35] K. Singh, A. Ohlan, V.H. Pham, R. Balasubramanian, S. Varshney, J. Jang, S. H. Hur, W.M. Choi, M. Kumar, S. Dhawan, *Nanoscale* 5 (2013) 2411–2420.
- [36] R. Patil, A.S. Roy, K.R. Anilkumar, K. Jadhav, S. Ekhelikar, *Comp. Part B: Eng.* 43 (2012) 3406–3411.
- [37] A. Lassoued, B. Dkhil, A. Gadri, S. Ammar, *Res. Phys.* 7 (2017) 3007–3015.
- [38] H. Mansour, H. Letifi, R. Bargougui, D. Almeida-Didry, B. Negulescu, C. Autret-Lambert, A. Gadri, S. Ammar, *Appl. Phys. A* 123 (2017) 1–10.
- [39] L. Munteanu, A. Munteanu, M. Sedlacik, E. Kutalkova, M. Kohl, A. Kalendova, *J. Ind. Eng. Chem.* 115 (2022) 440–448.
- [40] M. Duhan, R. Kaur, *J. Comp. Sci.* 5 (2020) 7.
- [41] Z. Morávková, I. Šeděnková, P. Bober, *Appl. Sci.* 10 (2020) 2091.
- [42] W. Xuelian, J. Jiang, Y. Jian, F. Qin, W. Zhifeng, *Des. Monomers Polym.* 24 (2021) 193–200.
- [43] S. Pani, S.K. Singh, B.K. Mohapatra, *Res. Geol.* 66 (2016) 12–23.
- [44] S. Ebrahim, R. El-Raey, A. Hefnawy, H. Ibrahim, M. Soliman, T.M. Abdel-Fattah, *Synth. Met.* 190 (2014) 13–19.
- [45] A. Korent, K.Ž. Soderžnik, S. Šturm, K.Ž. Rožman, *J. Electrochem. Soc.* 167 (2020) 106504.
- [46] A. Singh, A. Singh, S. Singh, P. Tandon, B. Yadav, R. Yadav, *J. Alloy. Comp.* 618 (2015) 475–483.
- [47] C. Wang, X. Tan, J. Yan, B. Chai, J. Li, S. Chen, *Appl. Surf. Sci.* 396 (2017) 780–790.
- [48] C.T.P. da Silva, V.L. Kupfer, G.R. da Silva, M.R. Moisés, P.A.G. Trindade, N.L. C. Domingues, A.W. Rinaldi, *Int. J. Electrochem. Sci.* 11 (2016) 5380.
- [49] B. Begum, S. Bilal, A.U.H.A. Shah, P. Röse, *Nanomaterials* 12 (2022) 513.
- [50] A. Eftekhari, *Sci. Direct Work. Pap.* (2000) 04.
- [51] L. Kilanski, S. Lewinska, A. Slawska-Waniewska, V.B. Pavlović, S. Filipović, *Inorg. Chem. Commun.* 145 (2022) 109960.
- [52] A.K. Ghasemi, M. Ghorbani, M.S. Lashkenari, N. Nasiri, *J. Energy Storage* 51 (2022) 104579.
- [53] S. Mondal, U. Rana, S. Malik, *J. Phys. Chem. C* 121 (2017) 7573–7583.
- [54] M. Mousa, M. Khairy, M. Shehab, *J. Solid State Electrochem.* 21 (2017) 995–1005.
- [55] Y. Xu, Z.-X. Xiao, Y. Yu, C. Yang, J.-Q. Yan, Huang, I. *Angew. Chem. Int. Ed.* 63 (2024) e202406054.
- [56] Z. Feng, X. Qiu, X. Chen, H. Wang, X. Guo, *Appl. Mat. Interfaces* 16 (2024) 42995.
- [57] M. Li, X. Qiu, T. Wie, Z. Dai, *Langmuir* 39 (2023) 8865.
- [58] X. Qiu, Q. Hua, L. Zheng, Z. Dai, *R.S.C. Adv.* 10 (2020) 5283–5293.
- [59] X. Zhang, D. Li, C. Dong, J. Shi, Y. Xu, *Mat. Today Commun.* 21 (2019) 100711.
- [60] M. Reda, S. Al-Ghannam, M. Al-Ghannam, *Adv. Mat. Phys. Chem.* 2 (2012) 75.